Bioresource Technology 442 (2026) 133697

Contents lists available at ScienceDirect

Bioresource Technology

journal homepage: www.elsevier.com/locate/biortech

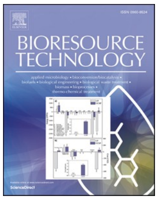

Engineering Ni(0)/Ni(II) interfaces in LDH-Derived Ni–Al catalysts for mild lignin depolymerization

Yanjun Wen [a,*], Wenxuan Li [a], Dmitry I. Sharapa [a], Thomas A. Zevaco [a], Dieter Schild [b], Felix Studt [a,c], Klaus Raffelt [a,*], Nicolaus Dahmen [a]

[a] Institute of Catalysis Research and Technology (IKFT), Karlsruhe Institute of Technology (KIT), Hermann-von-Helmholtz-Platz 1, Eggenstein-Leopoldshafen 76344, Germany
[b] Institute for Nuclear Waste Disposal (INE), Karlsruhe Institute of Technology (KIT), Hermann-von-Helmholtz-Platz 1, Eggenstein-Leopoldshafen 76344, Germany
[c] Institute for Chemical Technology and Polymer Chemistry (ITCP), Karlsruhe Institute of Technology (KIT), Engesserstr. 20, Karlsruhe 76131, Germany

HIGHLIGHTS

- A facile LDH co-precipitation method yielded highly active Ni(0)/Ni(II) interfacial catalysts.
- Dual-site Ni(0) and Ni(II) catalyst developed for lignin C-O activation.
- Complete (100 %) cleavage of β-O-4 linkages at 125 °C under mild conditions.
- In situ XAFS verified the coexistence of metallic Ni and NiO phases.
- DFT calculations revealed synergistic coupling between Ni(0) and Ni(II).

GRAPHICAL ABSTRACT

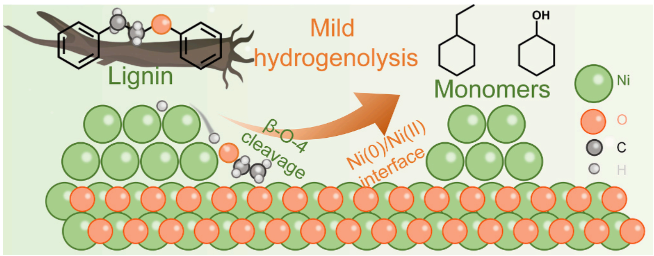

ARTICLE INFO

Keywords:
Biomass
β-O-4 lignin linkage
Depolymerization
Ni(0)/Ni(II) Interfaces
Catalytic hydrogenolysis

ABSTRACT

As the primary renewable reservoir of aromatic carbon, lignin motivates the development of efficient catalysts as a promising route to depolymerization under mild conditions. To address this challenge, layered double hydroxide (LDH) derived Ni–Al catalysts with varying Ni/Al ratios, engineering Ni(0)/Ni(II) interfaces, were developed. Beyond achieving complete β-O-4 conversion of the 2-phenethyl phenyl ether at 125 °C and 25 bar, outperforming previously reported noble- and non-noble-metal catalysts for this model compound, the catalyst also effectively depolymerizes organosolv lignin under 150 °C. A suite of characterizations, including in situ XAFS, confirmed the coexistence of Ni(0) and Ni(II) and the formation of Ni(0)/Ni(II) interfacial sites. Additionally, DFT calculations employing a Ni(1 1 1)/NiO(1 0 0) nanowire model showed that Ni(II) modulates the electronic structure of Ni(0), significantly enhancing its catalytic activity. Reaction pathways identified at the Ni (1 1 1)/NiO(1 0 0) interface exhibit superior thermodynamic and kinetic profiles relative to conventional Ni(1 1 1) surfaces. Combined experimental evidence and DFT analyses establish the Ni(0)/Ni(II) interface as the decisive active site enabling hydrogenolysis under mild conditions. This work provides an efficient platform for mild lignin depolymerization and elucidates the synergistic catalysis at the Ni(0)/Ni(II) interface, paving the way for sustainable biomass conversion.

---

* Corresponding authors.
E-mail addresses: wen.yanjun@kit.edu (Y. Wen), klaus.raffelt@kit.edu (K. Raffelt).

https://doi.org/10.1016/j.biortech.2025.133697
Received 17 September 2025; Received in revised form 16 November 2025; Accepted 23 November 2025

1. Introduction

Recently, the lignin-first strategy has gained popularity in biomass refining processes, not only because of its pivotal role in carbon emissions reduction but also as the sole natural source of aromatic rings (Sun et al., 2020; Liu et al., 2025; Jia et al., 2024; Lin et al., 2023). However, lignin, as a three-dimensional structured biopolymer, is difficult to utilize directly due to its disordered units, complex linkages, and high molecular weight (Chen et al., 2025; Luo et al., 2025; Shu et al. (2016) a). β-O-4 is the predominant linkage in the cleavage process of lignin, constituting 45–60 % of its structure and characterized by its relatively lower bond energy (Cai et al., 2023; Liu et al. (2024a); Rigo et al., 2025; Zhou et al., 2025). Therefore, targeting the β-O-4 linkage is paramount, yet efficient cleavage under mild conditions remains elusive.

Currently, various methods have been employed to cleave the β-O-4 bond, including hydrolysis, (Xue et al., 2020) oxidation, (Liu et al., 2022) the use of ionic liquids, (Xin et al., 2023) supercritical treatment, (Pérez et al., 2018) and biological and enzymatic strategies (Chauhan, 2020). Among these methods, hydrogenolysis holds significant industrial potential, offering numerous advantages such as high monomer yields and effectively preventing coke formation through saturation of reactive polycyclic structures. A wide range of catalytic systems, including noble metals, transition metals, and sulfidic catalysts, have been investigated for the β-O-4 hydrogenolysis process (Chio et al., 2019; Shen et al., 2024). As a mature industrial hydrogenation catalyst, Ni is an attractive choice due to its availability and connected cost-effectiveness. Zhou et al. explored the influence of lanthanum-modified Ni/CNT catalysts on β-O-4 cleavage and the hydrodeoxygenation process under 240 °C (Zhou et al., 2020). They confirmed that Brønsted acid sites play an important role through specific experiments and DFT calculations. Xu et al. investigated hydrogenolysis of a dimeric lignin model compound using Ni/ZnO-Al_2O_3 achieving high selectivity for ethylcyclohexane under 190 °C.(Xu et al., 2017) As harsh conditions are still typical for lignin hydrogenolysis, constructing Ni(0)/Ni(II) interfaces that couple H_2 activation on Ni(0) with C—O polarization and transition-state stabilization on Ni(II)/NiO is a logical strategy to lower the barriers and achieve mild operation.(Wang et al., 2023).

Layered double hydroxides (LDHs) provide a practical materials route to engineer adjacent Ni(0)/Ni(II) domains. In Ni–Al LDHs, tuning the M^{2+}/M^{3+} ratio and interlayer anions enables a topotactic transformation (LDH → mixed oxides, LDO) followed by H_2 reduction that yields metallic Ni in intimate contact with residual Ni(II) species. In contrast to conventional impregnation or co-precipitation routes, the LDH-derived approach provides intimately interfaced Ni/NiO domains with high dispersion and controllable Ni(0)/Ni(II) ratios. Under controlled reduction, a fraction of Ni(II) is retained due to strong metal–oxygen interactions and the oxygen/hydroxyl reservoir of the support, furnishing Ni(0)/Ni(II) interfaces. The density of Ni(0)/Ni(II) interfaces can be adjusted through composition and activation conditions, which underpins our experimental design. Beyond lignin chemistry, Kuhaudomlap's research into the effects of divalent Ni on furfural hydrogenation demonstrated that Ni(0) and Ni(II) produce a synergistic promotional effect (Kuhaudomlap et al., 2023). Similarly, Zhao et al. investigated the cooperative catalysis of Ni(0) and Ni (II) in converting nitrobenzene to aniline, proposing a mechanism where metallic Ni dissociates H_2 while Ni(II) adsorbs NO groups (Zhao et al., 2016). Although these reactions differ from lignin hydrogenolysis, they collectively motivate a Ni(0)/Ni(II) interfacial strategy to lower the barriers required for mild β-O-4 cleavage, providing the conceptual basis for the present work.

In this study, we investigated mild hydrogenolysis of the β-O-4 linkage using LDH-derived Ni–Al catalysts designed to create Ni(0)/Ni (II) interfaces. We synthesized catalysts with varied Ni/Al ratios by co-precipitation and used XPS, TEM, and in situ XAFS to verify coexisting Ni(0)/Ni(II) and to evidence interfacial sites under operating conditions. We evaluated catalytic activity on 2-phenethyl phenyl ether (PPE) as a β-O-4 model and extended the assessment to lignin under mild conditions. DFT comparisons between Ni(1 1 1) and Ni(1 1 1)/NiO(1 0 0) models elucidated how Ni(II) modulated the electronic structure of Ni (0) and lowered key barriers along the β-O-4 pathway. Taken together, these results supported the working hypothesis that the Ni(0)/Ni(II) interface was the key active site enabling mild hydrogenolysis.

2. Experimental section

2.1. Catalyst preparation

Ni-Al LDH Catalysts: Initially, $Ni(NO_3)_2{\cdot}6H_2O$, $Al(NO_3)_3{\cdot}9H_2O$, and urea were dissolved in deionized water and sonicated for 30 min. The solution was then transferred into a three-necked flask and stirred with a magnetic stirrer for 3 h to ensure uniform mixing. The mixture was subsequently heated to 100 °C in an oil bath and reacted for 12 h. After cooling to room temperature, the solution was washed until the pH reached 7. The precipitate was separated using a centrifuge and dried overnight in an oven at 70 °C. This Ni-Al LDH was then calcined at 500 °C for 3 h with a heating rate of 5 °C/min to form Ni-Al LDO. Finally, the Ni-Al LDO was reduced in a 10 % H_2/N_2 atmosphere under 500 °C for 2 h at a 5 °C/min heating rate.

Ni-Al Impregnation catalyst: First, $Ni(NO_3)_2{\cdot}6H_2O$ and commercial γ-Al_2O_3 were dispersed in deionized water and sonicated for 30 min. The solution was then placed into a single-necked flask and the water was removed using a rotary evaporator. Subsequently, the same drying, calcination, and reduction steps as the Ni-Al LDH catalyst were applied.

Ni-Al Precipitation catalyst: $Ni(NO_3)_2{\cdot}6H_2O$ and commercial Al_2O_3 were dissolved in deionized water and sonicated for 30 min. Then, 1 M NaOH was gradually added to the solution until the pH reached 10, followed by overnight stirring for aging. The solution was then washed with deionized water to completely remove Na ions, and the same drying, calcination, and reduction steps as the Ni-Al LDH catalyst were followed.

2.2. Catalytic performance test

Typically model compound for HDO experiments: 0.2 g of the model compound (PPE, acquired from VWR Chemicals), 0.2 g of the catalyst, and 20 g of the solvent (decalin, sourced from Sigma Aldrich) were placed into batch reactor. The catalyst test under different temperatures was performed under 25 bar (room temperature) H_2 and 1 h reaction time at the target temperature. Prior to each reaction, the reactor was purged three times with pure argon (Ar) to ensure complete removal of air. Throughout the reaction, the temperature was increased with a rate of 3.3 °C/min, and the mixture was stirred continuously at 600 rpm. After the reaction, the catalyst was removed through filtration and the liquid product was then analyzed using GC-MS (Agilent 6890 N with an Agilent 5973 N mass spectrometer) for compound identification and GC-FID (HP 5890 gas chromatograph equipped with an Rxi®5Sil MS capillary column, 0.25 μm × 0.25 μm × 30 m) for quantification of each compound.

2.3. DFT calculation

In this study, we performed slab model calculations utilizing the VASP (Kresse and Furthmüller, 1996a, 1996b) alongside the ASE (Bahn and Jacobsen, 2002). Exchange and correlation energies were derived using the PBE functional (Perdew et al., 1996). The vdW corrections were incorporated through the application of Grimme's DFT-D3 method (Grimme et al., 2010). Inner electrons were modeled using PAW pseudopotentials, (Blöchl, 1994; Kresse and Joubert, 1999) setting a cutoff energy at 450 eV. The Brillouin zone sampling was executed via a Γ-centered k-point mesh, generated employing the Monkhorst-Pack method. DFT + U ($U = 6.3$ eV) is employed to improve the description of systems with strongly correlated Ni 3d electrons in NiO (Rohrbach and Hafner, 2005). Geometry optimizations proceeded until the force on each atom diminished below the convergence threshold of 0.03 eV/Å, ensuring energy convergence within 10^{-6} eV. We employed the Climbing Image Nudged Elastic Band (CINEB)(Henkelman et al., 2000) and dimer methods to investigate the transition states of elemental reactions. All of the transition state structures were tested to make sure only one imaginary frequency, and the thermo energy correction was calculated by the package of VASPKIT (Wang et al., 2021).

3. Results and discussion

3.1. Catalyst characterization

Fig. 1a schematically outlines the synthesis of the Ni/NiO/Al_2O_3 catalyst derived from LDH structure via the coprecipitation method. Utilizing the properties of LDH, we can produce a series of catalysts with varying Ni contents by adjusting the Ni precursor ratio. Consequently, we have synthesized catalysts with high Ni content, achieving an optimal composition of up to 70 wt% Ni in this study. The variations in Ni content were quantified using inductively coupled plasma optical emission spectrometry (ICP-OES) (see Supplementary Material). The layered morphology of the Ni-Al LDH was analyzed by scanning electron microscopy (SEM), displaying an intriguing flower-like shape with petal thicknesses of approximately 10 nm, depicted in Figs. 1b,c. The layered morphology ensures uniform distribution of Ni-Al, which is corroborated by the SEM with energy dispersive X-ray spectroscopy (EDX) mapping results (see Supplementary Material). The successful synthesis of the LDH structure was further verified by X-ray diffraction (XRD) analysis, as shown in Fig. 2a, where characteristic peaks at 11.7°, 23.6°, and 35.2° indicate well-formed Ni-Al LDH crystalline particles. Upon calcination in air, the LDH was transformed into LDO and subsequently reduced in a 10 % H_2/N_2 atmosphere to produce the catalyst consisting of Ni based on Al_2O_3. As illustrated in Figs. 1d,e, the layered structure of the LDH was retained, confirming that the basic framework remained intact during thermal treatment. The layered characteristic layered pattern benefits subsequent annealing processes, preventing the unfavorable formation of overly large particles due to agglomeration. The XRD results displayed in Fig. 2a demonstrate the presence of NiO and

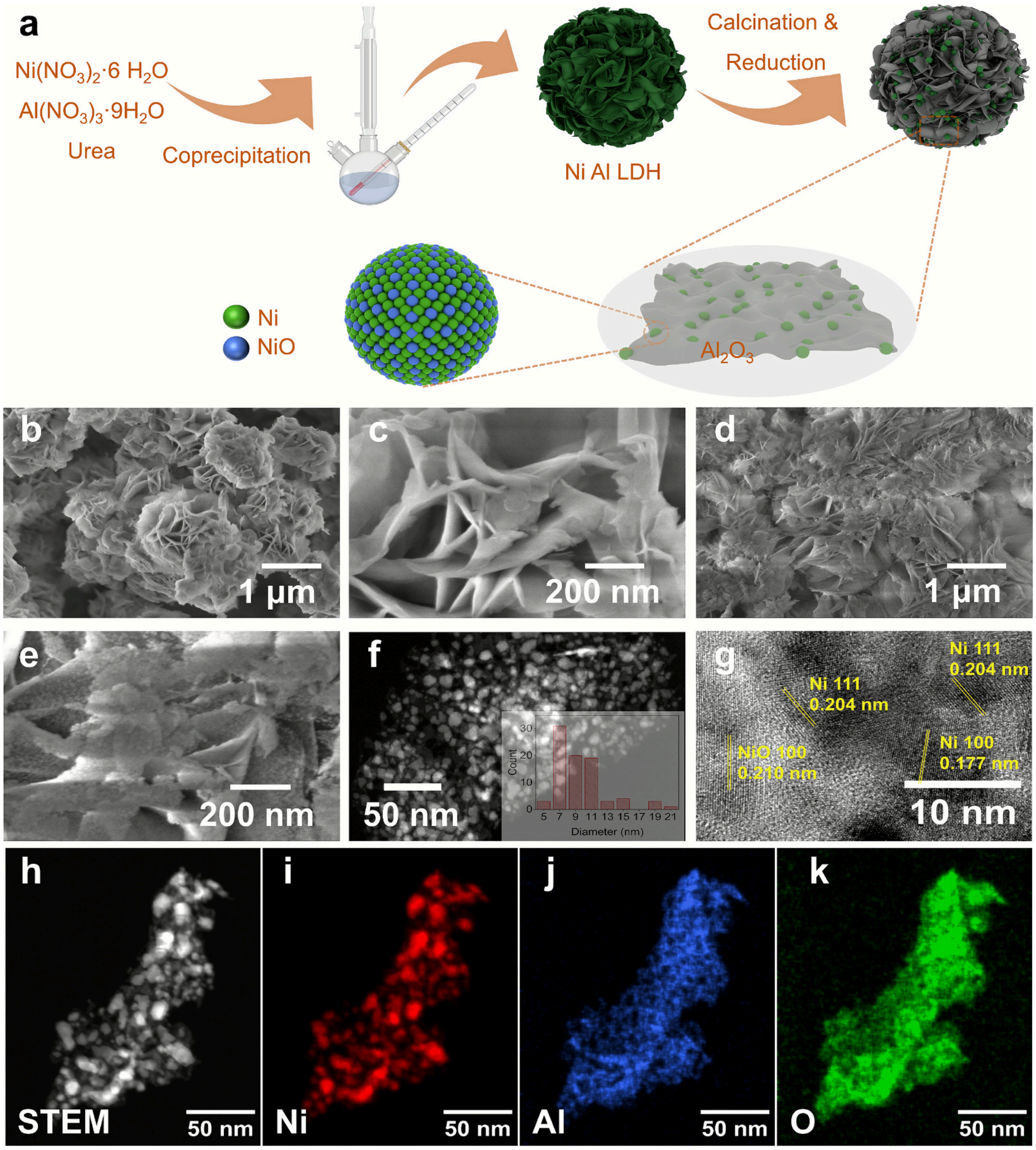

Fig. 1. A. schematic illustration of the synthesis of ni al catalyst derived from ldh structure; b, c. SEM images of Ni Al LDH structure; c, d. SEM images of Ni/Al catalyst; f. the TEM image of Ni/Al catalyst; g. High resolution TEM image of Ni/Al catalyst; h–i. EDX-mapping from TEM of Ni/Al catalyst.

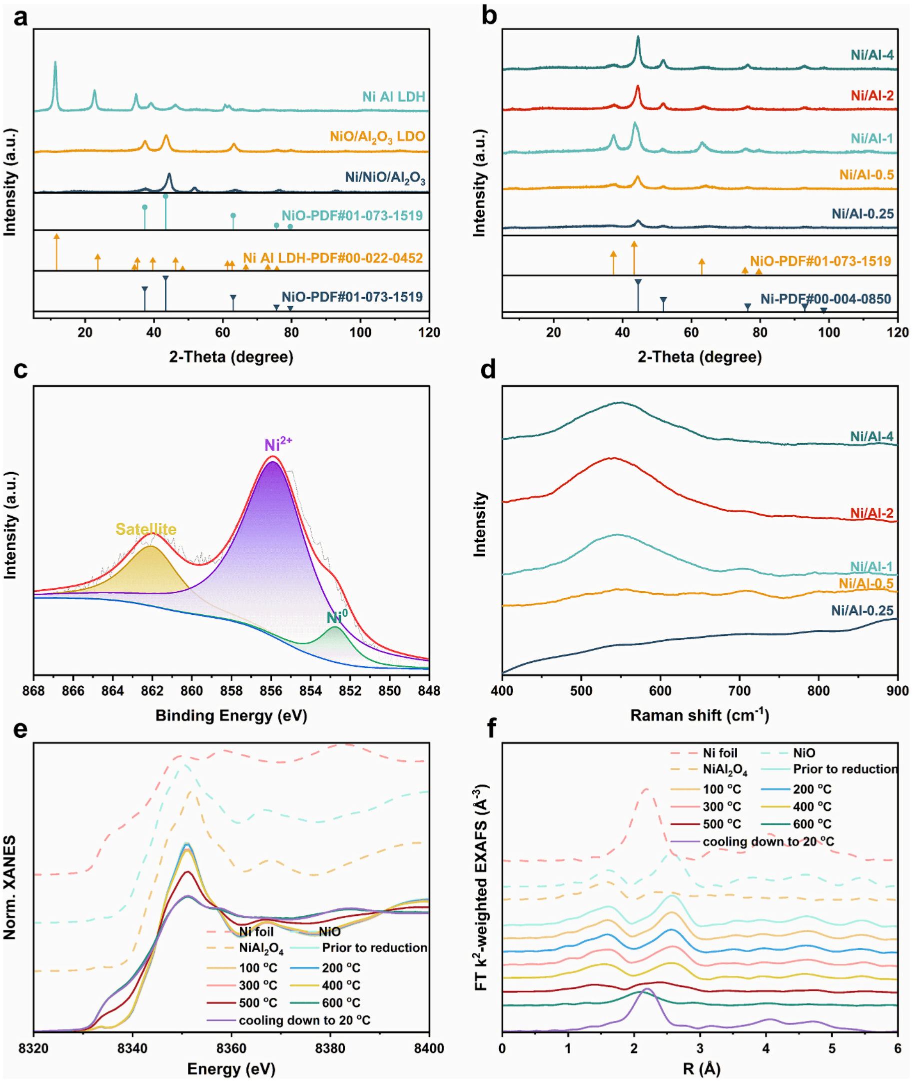

Fig. 2. A. xrd patterns of ni-al ldh, ni-al ldo, and ni/al-2 catalyst after reduction; b. XRD patterns of different Ni/Al ratio catalysts; c. Ni 2p High resolution XPS spectra for Ni/Al catalyst; d. Raman spectra for different Ni/Al ratio catalysts; e. Normalized Ni K edge XANES spectra of the Ni/Al-2 catalyst and selected Ni reference compounds; f. Fourier-transformed k2-weighted Ni K edge EXAFS spectra of the Ni/Al-2 catalyst during reduction and selected Ni reference compounds.

Al_2O_3 after the reduction, confirming the successful transformation of Ni-Al layered double oxide (LDO) into Ni, NiO, and Al_2O_3. Specifically, within the LDO spectrum, peaks corresponding to NiO are observed at 37.3°, 43.4°, and 63.0°. Additionally, peaks indicative of Ni are detected at 44.5° and 51.8°. However, the characteristic peaks for Al_2O_3 are not distinctly visible, possibly due to its poor crystallinity. Transmission electron microscopy (TEM) images shown in Fig. 1f provide a more detailed depiction of the catalyst's morphology compared to SEM images, revealing white particles embedded within a grey matrix. It is hypothesized that the grey matrix consists of a partly amorphous Al_2O_3 framework, while the white particles contain a high amount of Ni. The particle size distribution, depicted in Fig. 1f (subfigure), is relatively uniform, primarily ranging from 7 to 11 nm, indicating a good homogeneity. Subsequent elemental distribution analyses, presented in Fig. 1h–k, confirm the grey matrix as composed of aluminum and oxygen, thus validating it as Al_2O_3. The areas with white particles predominantly show distributions of Ni and oxygen. Combined with XRD results, these findings suggest that the white particles are a mixture of Ni and NiO.

Interestingly, NiO was still present along with Ni after the reduction process, as confirmed through various analytical methods. Analysis of XRD patterns (Fig. 2b) revealed characteristic diffraction peaks attributable to both metallic Ni and NiO phases. In the sample with the lowest Ni loading (Ni/Al-0.25), these reflections exhibited notable peak broadening and relatively low intensity, indicative of smaller crystallite dimensions and enhanced dispersion of Ni-based species. With increasing Ni/Al ratios (from Ni/Al-0.5 to Ni/Al-4), the characteristic Ni diffraction peaks progressively evolved, displaying enhanced sharpness and intensity, suggesting increased crystallite size or higher overall Ni content. The concurrent presence of NiO reflections confirmed the coexistence of both Ni(0) and Ni(II) species. Significantly, NiO diffraction peaks were exclusively detected in samples with Ni/Al ratios exceeding 1, suggesting that elevated Ni concentrations facilitate the detection of residual NiO following the reduction process. The Ni 2p X-ray photoelectron spectroscopy (XPS) spectrum (Fig. 2c) reveals a complex peak structure consisting of a distinct peak at 852 eV, a dominant peak at 856 eV, and a characteristic satellite feature at higher binding energies (~862 eV) (Xu et al., 2024). Based on reference binding energies from literature, the peak at 852 eV can be assigned to metallic nickel, while the peak at 856 eV is characteristic of Ni(II) species. The presence of the satellite peak at 862 eV, a distinctive spectral feature of Ni(II), provides additional confirmation of the oxidized nickel species in the sample. These spectral features demonstrate the coexistence of both metallic and oxidized nickel species on the catalyst surface.

This observation suggests that during the synthesis or subsequent treatment processes, nickel underwent partial reduction, resulting in a mixed-valence state rather than complete conversion to the metallic form. Then according to Raman spectroscopy results depicted in Figs. 2d, a peak at approximately 550 cm^{-1} corresponds to NiO, whereas Ni showed no signal, corroborating the XRD findings that NiO remained (Wang et al., 2025). Lastly, HRTEM (High-Resolution Transmission Electron Microscopy) results presented in Fig. 1g demonstrate different lattice spacings; measurements identified various exposed facets of Ni and NiO, confirming the coexistence of metallic and ionic Ni on the surface. The H_2-TPR results (see Supplementary Material) of the Ni/Al-2 catalyst also confirmed that it has a reduction peak at 700 °C, which indicates that the reduction conditions at 500 °C are insufficient to completely reduce all NiO. This indirectly validates the reasonable coexistence of Ni(0) and Ni(II).

In situ X-ray absorption spectroscopy (XAS) analysis was performed to elucidate the evolution of Ni species under reducing conditions during thermal treatment from ambient temperature to 600 °C in a H_2/He atmosphere. The in situ X-ray absorption near-edge structure (XANES) spectra (Fig. 2e) exhibited systematic changes in both the absorption edge position and white line intensity with increasing temperature, indicating the progressive reduction of NiO-like species to metallic Ni. The observed edge position shift toward that of the Ni foil reference suggested an increasing proportion of Ni(0). However, the incomplete overlap between the sample spectra and the Ni foil standard at 600 °C indicated the persistence of Ni(II). This interpretation was corroborated by the white line intensity, which remained elevated compared to the metallic reference. Quantitative analysis through linear combination fitting of the XANES data (see Supplementary Material) revealed that at 500 °C, the sample comprised 56.8 % Ni(II) and 43.2 % Ni(0). Subsequent heating to 600 °C resulted in a decrease in Ni(II) content to 20.7 %, demonstrating the progression of the reduction process. The structural evolution was further characterized by Fourier-transformed (FT) k^3-weighted extended X-ray absorption fine structure (EXAFS) analysis (Fig. 2f), complemented by k^2-weighted EXAFS spectra (see Supplementary Material). With increasing reduction temperature, the Ni–O coordination peak (characteristic of NiO at ~ 1.6 Å) diminished in intensity, while the Ni–Ni peak (approximately 2.5 Å) intensified, consistent with the progressive transformation of the NiO lattice to metallic Ni under H_2 atmosphere. The persistent Ni–O feature in the EXAFS spectrum at maximum temperature indicated incomplete reduction. First-shell EXAFS fitting of the sample at 600 °C (and after cooling to ambient temperature) yielded Ni–O coordination numbers of 1.1–1.3 (see Supplementary Material). These results quantitatively confirmed approximately 80 % reduction of Ni, supporting the coexistence of metallic and oxidized nickel species. Ni K-edge WT (Wavelet-transform) maps (see Supplementary Material) reveal that the Ni/Al-2 catalyst reduced at 400 °C is dominated by a low-k band at $R' \approx 1.5$ Å, assigned to the Ni–O first coordination shell, and a high-k feature appears at $R' \approx 2.7$ Å from the Ni–Ni second shell, indicating a largely oxidized state. Upon heating to 500 °C, the metallic Ni–Ni first-shell signal at $R' \approx 2.3$ Å strengthens markedly, whereas Ni–O first shell and Ni–Ni second shell remain detectable, evidencing the coexistence of metallic Ni and oxygen-coordinated Ni species and thus abundant interfacial sites. Further increasing the temperature to 600 °C renders the metallic Ni–Ni first shell dominant and the Ni–O contribution nearly disappears; the pattern approaches that of Ni foil, consistent with particle growth and enhanced metallic connectivity.

The comprehensive in situ XANES and EXAFS analyses demonstrated that while the formation of metallic Ni proceeded with increasing reduction temperature, a significant fraction of NiO remained stable. These findings establish that the catalyst maintains a dual-phase composition of Ni(0) and Ni(II) after reduction treatment under the specified conditions.

3.2. Hydrogenolysis of PPE

The catalytic performance was evaluated through PPE hydrogenolysis experiments. Initially, catalysts prepared by various methods were evaluated. According to Fig. 3a, the Ni/Al-2 catalysts derived from the LDH structure exhibited superior performance, requiring only 125 °C to achieve the desired outcome. In contrast, catalysts prepared via wet impregnation and co-precipitation methods required a minimum temperature of 180 °C, with complete conversion requiring a temperature of 220 °C. Notably, the Ni/Al-2 sample reduced at 400 °C was predominantly NiO with negligible Ni(0) (see Supplementary Material) and showed no activity at 125°. Taken together, these observations suggest that neither purely NiO nor fully metallic Ni is optimal under mild conditions; rather, the superior activity of the LDH-derived catalyst at 125 °C likely originates from the coexistence of Ni and NiO—i.e., Ni–NiO interfacial sites. Then, the Ni/Al catalyst derived from LDH was compared with other catalysts reported in the literatures (Fig. 3b) (Bjelic et al., 2020; Luo et al., 2016; Lv et al., 2022; Salam et al., 2021; Yang et al., 2022; Zhang et al., 2020). For the hydrogenolysis of PPE, Ru is commonly used as the active metal; however, non-noble transition metals like Ni typically require higher temperatures. In our work, by adjusting the presence of Ni(0) and Ni(II), the Ni/Al materials derived from LDH catalyst exhibited high catalytic activity under mild conditions. Detailed conditions of these experiments are summarized (see Supplementary Material).

Subsequently, catalysts with varying Ni/Al ratios were evaluated, shown in Fig. 3c. It was observed that conversion rates increased with the Ni/Al ratio, achieving complete conversion when the ratio exceeded 1. This improvement may be attributed to the absence of the NiO phase when the Ni/Al ratio was below 0.5. Specifically, in the hydrogenolysis of PPE, the catalyst with a Ni/Al ratio of 2 showed minimal dimer formation and exhibited the highest selectivity for monomers. This indicates that the synergistic effect between Ni(0) and Ni(II) is optimal when the Ni/Al ratio is 2. Moreover, the majority of the products were fully hydrogenated benzene derivatives, suggesting that aromatic compounds are less likely to persist under stringent hydrogen conditions. Given that ring saturation is typically metal-driven, the shift from ethylbenzene to ethylcyclohexane at higher temperature is most consistent with enhanced hydrogenation on Ni(0) under H_2. The acidic contribution (from the Al_2O_3 matrix/residual hydroxyls) is considered secondary, potentially assisting in hydrolysis/methanolysis of β-O-4 intermediates rather than in direct ring hydrogenation. Finally, the Ni/Al LDH-derived catalyst with a ratio of 2 was tested at various temperatures, as depicted in Fig. 3d. At 100 °C, no catalytic activity was observed. However, when the temperature exceeded 125 °C, the conversion rate reached 100 %. In terms of product selectivity, an increase in temperature led to a higher formation of dimer byproducts. The dimer fraction is plausibly derived from condensation of benzyl/phenoxy intermediates on acid sites, rather than unconverted PPE. This view is consistent with the simultaneous rise of ring-hydrogenated species and suggests a temperature-activated competition between C—O scission/hydrogenation and acid-promoted coupling. Additionally, the product transitioned from ethylbenzene to the fully hydrogenated product ethylcyclohexane. This demonstrates that the catalyst exhibits optimal hydrogenolysis performance under relatively mild conditions. Overall, a working network can be outlined: (i) β-O-4 hydrolysis/methanolysis to cleavable fragments; (ii) hydrogenolysis at Ni(0)/Ni(II) interfaces to form phenolic/aryl products; (iii) subsequent ring hydrogenation on Ni(0) yielding ethylcyclohexane; and (iv) acid-assisted condensation of benzyl/phenoxy intermediates leading to dimers. The stability of the Ni/Al-2 catalyst was evaluated (see Supplementary Material), which exhibited excellent durability, maintaining a conversion rate of over 93 % after five consecutive cycles. Finally, The Ni/Al-2 catalyst was applied to a real organosolv lignin (obtained via hydrothermal treatment at 220 °C) to evaluate its hydrogenolysis activity. The composition distributions of the feedstock and the reaction products by GC-MS (Fig. 3e),

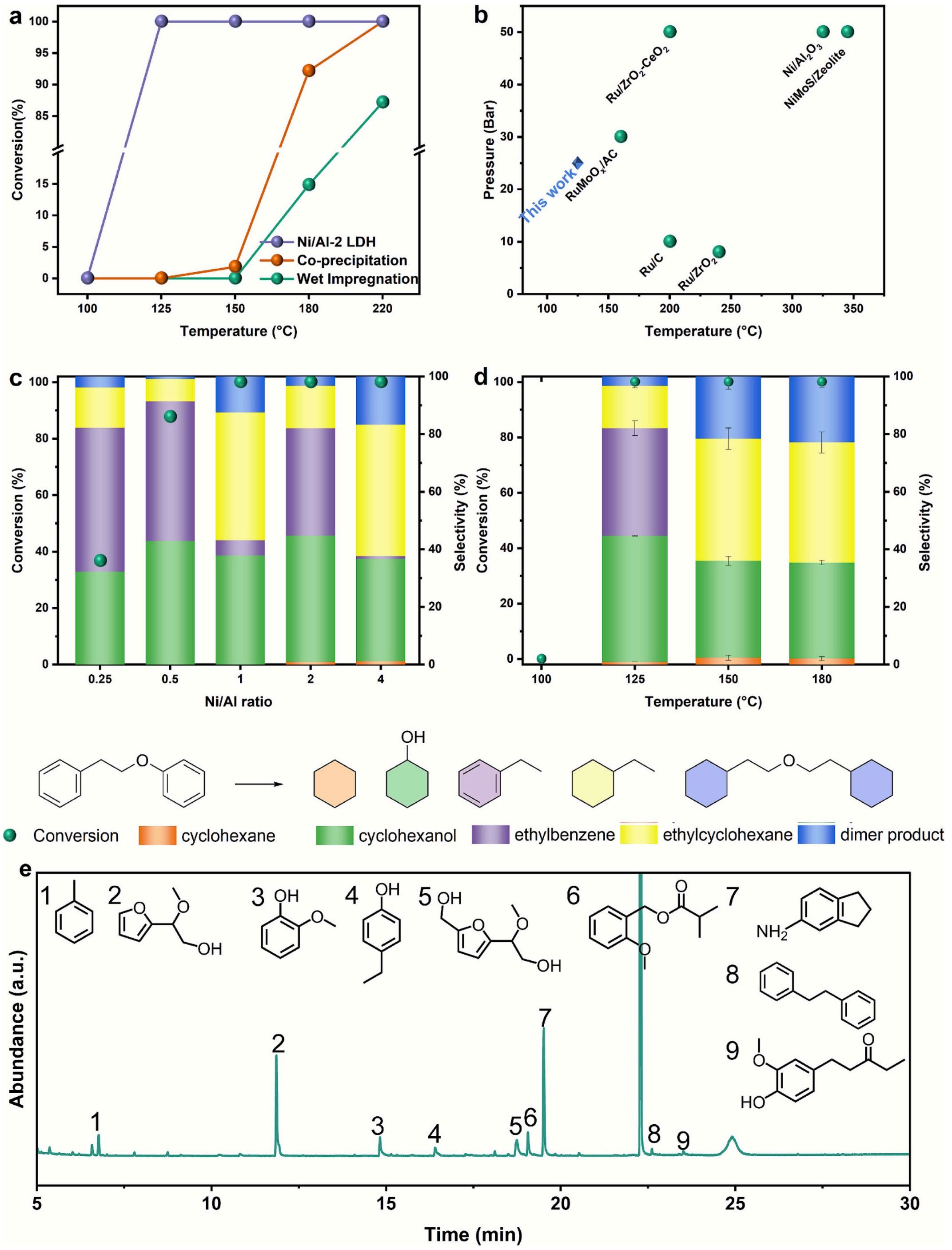

Fig. 3. A. The conversion of PPE Hydrogenolysis over Ni/Al catalysts prepared by different methods at various temperature. Reaction conditions: 0.2 g PPE, 0.2 g Catalyst, 20 g decalin, 25 bar H_2, 1 h; b. Comparison of PPE hydrogenolysis conditions from different literatures; c. The conversion and selectivity of PPE hydrogenolysis over different Ni-Al ratio catalysts. Reaction conditions: 0.2 g PPE, 0.2 g Catalyst, 20 g decalin, 125 °C, 25 bar H_2, 1 h; d. The conversion and selectivity of PPE hydrogenolysis over Ni/Al-2 catalyst at various temperature. Reaction conditions: 0.2 g PPE, 0.2 g Catalyst, 20 g decalin, 25 bar H_2, 1 h; e. Product distribution from the hydrogenolysis of organosolv lignin over Ni/Al-2 as determined by GC–MS. Reaction conditions: 0.2 g lignin, 0.2 g Catalyst, 25 g methanol, 150 °C, 25 bar H_2, 2 h.

GPC and NMR (see Supplementary Material) indicate that part of the lignin was hydrogenolyzed to phenolic monomers, yield 5.7 %, together with a small fraction of dimers. The reaction was conducted at 150 °C under 25 bar H_2 for 2 h. Compared with prior studies on lignin hydrogenolysis, this yield is relatively low, which is attributable to the lower reaction temperature and the limited reaction time employed here (Luo et al., 2025; Shen et al., 2017; Shu et al., 2016b). Nevertheless, these results demonstrate that the Ni/Al-2 catalyst remains effective and promising for the depolymerization of real lignin.

3.3. DFT Calculation

DFT calculations were used to investigate reaction mechanism and the synergistic interaction bewteen Ni(0) and Ni(II). The stable low-index facets, 111 and 100, are utilized for modeling Ni and NiO, respectively (see Supplementary Material). Combined TEM, XRD, and

XAS analyses reveal the coexistence of Ni and NiO, highlighting the need to interrogate the Ni(0)/Ni(II) interface. However, conventional cluster models contain under-coordinated metal atoms that can spuriously enhance apparent reactivity. To mitigate this artifact and better represent realistic coordination at the interface, a Ni(1 1 1)/NiO(1 0 0) nanowire model was adopted for the simulations.(Polierer et al., 2019; Whittaker et al., 2018; Zhao et al., 2017) To simplify the computations, the effects of varying the number of NiO layers were examined. The comparative analysis of three-layer and two-layer NiO configurations on reactant adsorption energies revealed only a minor difference of 0.1 eV. Furthermore, the stability of Ni nanowire on various adsorption sites was tested (see Supplementary Material), with results indicating that the most stable configuration involved Ni bonding with oxygen on the NiO surface. Consequently, a model comprising a two-layer NiO(1 0 0) with a three-layer Ni nanowire was adopted, as depicted in Fig. 4a.

Subsequently, to explore the influence of NiO on the electronic structure of Ni, the density of states (DOS) for both Ni(111) and the Ni (111)/NiO(100) nanowire were compared. The partial density of states (PDOS) for their 3d orbitals is presented in Fig. 4b. Around − 2 eV, the electronic state peak position of Ni(1 1 1)/NiO(1 0 0) shifts compared to that of Ni(111), indicating that Ni is influenced by the underlying NiO layer, leading to modifications in its electronic structure. Furthermore, the results suggest that the 3d orbitals of Ni(1 1 1)/NiO(1 0 0) become more localized. Since Ni is not in a purely metallic state in this system, its orbital occupancy and energy distribution shift towards higher energy levels, causing the d-band center to move to lower energies. The shift of the d-band center is typically associated with changes in surface reaction activity; generally, when it is closer to the Fermi level, the system exhibits higher activation capability. Then ELF analysis (see Supplementary Material) indicates reduced electron delocalization for Ni at the Ni (1 1 1)/NiO(1 0 0) interface relative to Ni(1 1 1), consistent with an electropositive Ni$^{\delta+}$ character. Charge density difference (See supplementary materials Fig. S18) together with Bader analysis (see Supplementary Material) further show a net transfer of ~ 1.69 electrons from interfacial Ni to the NiO overlayer, predominantly localized within the immediate contact layer. Taken together, these charge analyses indicate that electron-depleted interfacial Ni$^{\delta+}$ exhibits exhibit higher catalytic activity and, owing to its Lewis acidity, more readily polarize C—O bonds to achieve their cleavage.

Subsequently, we assessed the adsorption energies of PPE on Ni(1 1

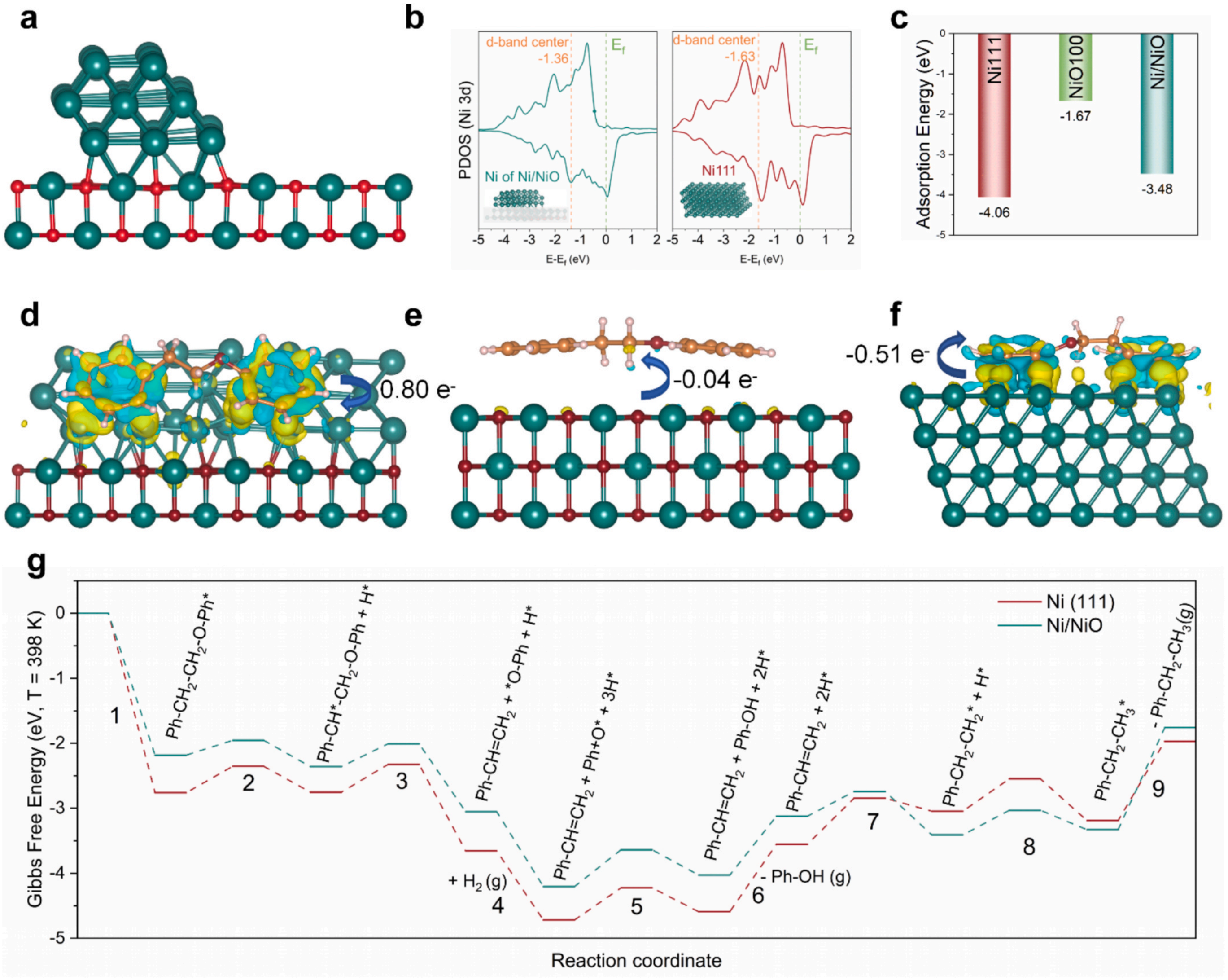

Fig. 4. A. the ni(1 1 1)/nio(1 0 0) nanowire model; b. pdos andd-band center of Ni supported on NiO and Ni(111); c. Comparison of adsorption energies over Ni(1 1 1), NiO(1 0 0), and Ni(1 1 1)/NiO(100); d–f. Charge density difference of PPE adsorption on slab of Ni(1 1 1)/NiO(1 0 0) (d), NiO(1 0 0) (e), and Ni(1 1 1) (f); The blue (yellow) distribution corresponds to charge accumulation (depletion), and the black value represent the number of electron transfers in Bader charges; The Ni, O, C, H atoms are presented as green, red, orange and pink, respectively; g. The Gibbs Free energy diagram of PPE hydrogenolysis over Ni(1 1 1)/NiO(1 0 0) and Ni(1 1 1) under 398 K (125 °C), the numbers 1–9 represent the elementary steps (see Supplementary Material).

1), NiO(1 0 0), and Ni(1 1 1)/NiO(1 0 0) (see Supplementary Material), while the optimal adsorption energies are illustrated in Fig. 4c. Here, NiO exhibited the lowest adsorption energy, with higher values observed for Ni(1 1 1) and Ni(1 1 1)/NiO(1 0 0). Since the adsorption energy of PPE is primarily contributed by the benzene ring, we utilized benzene as a test case to validate our adsorption energy calculations. Previous DFT calculations and experimental studies have established that the adsorption energy of monocyclic aromatic hydrocarbons and their derivatives on Ni(1 1 1) typically ranges from − 2.0 to − 2.4 eV.(Jia and An, 2018; Liu et al. (2024b)) For instance, the experimentally determined adsorption energy of benzene on Ni(1 1 1) is reported as − 2.13 eV.(Cox et al., 1970) In our study, we calculated an adsorption energy of − 2.03 eV (see Supplementary Material), which demonstrates excellent agreement with both experimental data and previous DFT results. Furthermore, considering that adsorption of monocyclic aromatics on metal surfaces follows a trend where a lower d-band center corresponds to stronger adsorption, one would anticipate Ni(1 1 1)/NiO(1 0 0) to exhibit more robust adsorption than Ni(1 1 1).(Hammer and Nørskov, 2000; Toyoda et al., 2009) To further explore their charge transfer characteristics, we conducted charge density difference and Bader charge analysis (see Supplementary Material), the results of which are shown in Fig. 4d–f. From the charge distribution, we observed significant charge transfer during PPE adsorption on both Ni(1 1 1) and Ni (1 1 1)/NiO(1 0 0) nanowire, indicating strong chemical adsorption. In contrast, the charge transfer between NiO(1 0 0) and PPE was weaker, suggesting physisorption. Bader charge analysis further revealed electron transfers of 0.51 and 0.80 electrons from Ni(1 1 1) and Ni(1 1 1)/NiO(1 0 0) nanowire surfaces to PPE, respectively, while NiO showed negligible electron transfer.

Therefore, we calculated the reaction pathway diagram (Fig. 4g) for PPE hydrogenolysis using both the Ni(111) and Ni-NiO models. Guided by prior results that C—O cleavage initiates with dehydrogenation, dehydrogenation barriers at representative sites were first evaluated (see Supplementary Material) (Wen et al., 2025). On both Ni(1 1 1) and the Ni(111)/NiO(100) interface, the preferred initial step follows the same pathway: Ph–CH_2–CH_2–O–Ph → Ph–CH–CH_2–O–Ph*, where Ph denotes phenyl ring. The detailed reaction steps involved in this process, energies of intermediates, and the relevant transition state structures are summarized (see Supplementary Material). Overall, the reaction is exothermic, with a Gibbs free energy change (ΔG) of − 1.75 eV at 398 K. Comparing the Ni(1 1 1) and Ni(1 1 1)/NiO(1 0 0) systems, the Ni(1 1 1)/NiO(1 0 0) exhibits a smoother energy variation during the fundamental hydrogenolysis steps of PPE, making it thermodynamically more favorable. Additionally, in the desorption steps of the products, Ni(1 1 1)/NiO(1 0 0) shows a greater thermodynamic change, indicating that the monomeric products may be more challenging to desorb, facilitating further hydrogenation and saturation of the benzene rings. The energy barrier for the C—O bond cleavage in PPE is only 0.35 eV on Ni(1 1 1)/NiO(1 0 0), compared to Ni(1 1 1), suggesting a lower kinetic barrier. This finding also corroborates the experimental results, where catalysts prepared via wet impregnation and coprecipitation, as well as the Ni/Al-0.25 LDH catalyst, were unable to activate the C—O bond cleavage process at 125 °C (398 K) due to the absence of NiO. Furthermore, for the hydrogenation of monomeric intermediates after cleavage, Ni(1 1 1)/NiO(1 0 0) exhibits a lower energy barrier compared to Ni(1 1 1). This suggests that Ni(0)/Ni(II) facilitates a faster conversion of intermediates, thereby enhancing the overall reaction rate.

4. Conclusions

In this study, a series of Ni/Al catalysts derived from LDH structures were successfully synthesized with varying ratios. Among them, the Ni/Al-2 catalyst achieved complete PPE conversion under relatively mild conditions (125 °C, 25 bar) and notably depolymerized organosolv lignin under same conditions. In the catalyst characterization analysis, both Ni(0) and Ni(II) were confirmed to still be present after reduction. Therefore, mechanistic investigations revealed that the presence of NiO altered the surface charge distribution of Ni, which in turn shifted the d-band center. This change affected the adsorption energy of PPE on the Ni (1 1 1)/NiO(1 0 0) surface and significantly influenced the cleavage barrier of the β-O-4 bond, facilitating the overall catalytic process. This study not only presents a highly efficient catalyst for the hydrogenolysis of biomass dimers under mild conditions but also sheds light on the synergistic catalytic interactions between Ni(0) and Ni(II).

CRediT authorship contribution statement

Yanjun Wen: Writing – original draft, Methodology, Investigation, Conceptualization. **Wenxuan Li:** Methodology, Investigation. **Dmitry I. Sharapa:** Writing – review & editing, Supervision. **Thomas A. Zevaco:** Methodology. **Dieter Schild:** Methodology. **Felix Studt:** Writing – review & editing, Supervision. **Klaus Raffelt:** Writing – review & editing, Supervision, Funding acquisition, Conceptualization. **Nicolaus Dahmen:** Supervision.

Declaration of competing interest

The authors declare that they have no known competing financial interests or personal relationships that could have appeared to influence the work reported in this paper.

Acknowledgment

The authors acknowledge support by the state of Baden-Württemberg through bwHPC and the German Research Foundation (DFG) through grant no INST 40/575-1 FUGG (JUSTUS 2 cluster) and bwunicluster. We acknowledge DESY (Hamburg, Germany), a member of the Helmholtz Association HGF, for the provision of experimental facilities. Parts of this research were carried out at the light source PETRA III at DESY, a member of the Helmholtz Association (HGF). We would like to thank Dr. Edmund Welter for his assistance in using the beamline P65. Beamtime was allocated for proposal II-20230692.

Appendix A. Supplementary material

Supplementary data to this article can be found online at https://doi.org/10.1016/j.biortech.2025.133697.

Data availability

Data will be made available on request.

References

Bahn, S.R., Jacobsen, K.W., 2002. An object-oriented scripting interface to a legacy electronic structure code. Comput. Sci. Eng. 4, 56–66. https://doi.org/10.1109/5992.998641.

Bjelic, A., Likozar, B., Grilc, M., 2020. Scaling of lignin monomer hydrogenation, hydrodeoxygenation and hydrocracking reaction micro-kinetics over solid metal/acid catalysts to aromatic oligomers. Chem. Eng. J. 399. https://doi.org/10.1016/j.cej.2020.125712.

Blöchl, P.E., 1994. Projector augmented-wave method. Phys. Rev. B 50, 17953–17979. https://doi.org/10.1103/PhysRevB.50.17953.

Cai, C., Li, N., Liu, H., Zhang, J., Zhu, J.Y., Wang, F., 2023. Extracting high β-O-4 content lignin and by-producing substrate susceptible to enzymatic hydrolysis by a green flow through process. Chem. Eng. J. 453, 139730. https://doi.org/10.1016/j.cej.2022.139730.

Chauhan, P.S., 2020. Role of various bacterial enzymes in complete depolymerization of lignin: a review. Biocatal. Agric. Biotechnol. 23, 101498. https://doi.org/10.1016/j.bcab.2020.101498.

Chen, D., Liu, J., Liu, B., Qin, Y., Lin, X., Qiu, X., 2025. Molecular weight engineering modulates lignin-metal supramolecular framework to construct carbon-coated CoRu alloy for effective overall water splitting. Adv. Mater. 37, 2501113. https://doi.org/10.1002/adma.202501113.

Chio, C., Sain, M., Qin, W., 2019. Lignin utilization: a review of lignin depolymerization from various aspects. Renew. Sustain. Energy Rev. 107, 232–249. https://doi.org/10.1016/j.rser.2019.03.008.

Cox, John D., Pilcher, G., Cox, John Desmond, 1970. Thermochemistry of organic and organometallic compounds. Acad. Press, London.

Grimme, S., Antony, J., Ehrlich, S., Krieg, H., 2010. A consistent and accurate *ab initio* parametrization of density functional dispersion correction (DFT-D) for the 94 elements H-Pu. J. Chem. Phys. 132, 154104. https://doi.org/10.1063/1.3382344.

Hammer, B., Nørskov, J.K., 2000. Theoretical surface science and catalysis—calculations and concepts, in: Advances in Catalysis. Elsevier, pp. 71–129. doi:10.1016/S0360-0564(02)45013-4.

Henkelman, G., Uberuaga, B.P., Jónsson, H., 2000. A climbing image nudged elastic band method for finding saddle points and minimum energy paths. J. Chem. Phys. 113, 9901–9904. https://doi.org/10.1063/1.1329672.

Jia, X., An, W., 2018. Adsorption of monocyclic aromatics on transition metal surfaces: insight into variation of binding strength from first-principles. J. Phys. Chem. C 122, 21897–21909. https://doi.org/10.1021/acs.jpcc.8b06321.

Jia, Z., Hu, J., Lu, P., Wang, Y., 2024. Carbon quantum dots from carbohydrate-rich residue of birch obtained following lignin-first strategy. Bioresour. Technol. 408, 131206. https://doi.org/10.1016/j.biortech.2024.131206.

Kresse, G., Furthmüller, J., 1996a. Efficiency of ab-initio total energy calculations for metals and semiconductors using a plane-wave basis set. Comput. Mater. Sci 6, 15–50. https://doi.org/10.1016/0927-0256(96)00008-0.

Kresse, G., Furthmüller, J., 1996b. Efficient iterative schemes for ab initio total-energy calculations using a plane-wave basis set. Phys. Rev. B 54, 11169–11186. https://doi.org/10.1103/PhysRevB.54.11169.

Kresse, G., Joubert, D., 1999. From ultrasoft pseudopotentials to the projector augmented-wave method. Phys. Rev. B 59, 1758–1775. https://doi.org/10.1103/PhysRevB.59.1758.

Kuhaudomlap, S., Mekasuwandumrong, O., Praserthdam, P., Lee, K.M., Jones, C.W., Panpranot, J., 2023. Influence of highly stable Ni $^{2+}$ species in Ni phyllosilicate catalysts on selective hydrogenation of furfural to furfuryl alcohol. ACS Omega 8, 249–261. https://doi.org/10.1021/acsomega.2c03590.

Lin, X., Liu, J., Qiu, X., Liu, B., Wang, X., Chen, L., Qin, Y., 2023. Ru−FeNi alloy heterojunctions on lignin-derived carbon as bifunctional electrocatalysts for efficient overall water splitting. Angew. Chem. 135, e202306333. https://doi.org/10.1002/ange.202306333.

Liu, C., Wen, C., Zhang, Z., Chen, Y., Yang, H., Li, J., Lian, C., Liu, H., 2024a. Adsorption variations on the Ni(111) surface: electron density diversity from oxygen-containing functional groups. Mol. Syst. Des. Eng. 9, 477–489. https://doi.org/10.1039/D3ME00168G.

Liu, J., Qiu, X., Sun, S., Liu, B., Tian, Y., Qin, Y., Lin, X., 2024b. Synthesis of highly dispersed carbon-encapsulated Ru–FeNi nanocatalysts by a lignin–metal supramolecular framework strategy for durable water-splitting electrocatalysis. Green Chem. 26, 8020–8029. https://doi.org/10.1039/D4GC01788A.

Liu, X., Wang, L., Zhai, L., Wu, C., Xu, H., 2022. H_2O_2-promoted C–C bond oxidative cleavage of β-O-4 lignin models to benzanilides using water as a solvent under metal-free conditions. Green Chem. 24, 4395–4398. https://doi.org/10.1039/D2GC00878E.

Liu, Z.-H., Liu, H., Xu, T., Zhao, Z.-M., Ragauskas, A.J., Li, B.-Z., Yuan, J.S., Yuan, Y.-J., 2025. Lignin valorization reshapes sustainable biomass refining. Renew. Sustain. Energy Rev. 211, 115296. https://doi.org/10.1016/j.rser.2024.115296.

Luo, B., Tian, Z., Shu, R., Wang, C., Chen, Y., Liu, J., Liao, Y., 2025. Highly stable biochar-encapsulated CoTi@BC nanocatalysts for lignin hydrogenolysis. J. Catal. 442, 115914. https://doi.org/10.1016/j.jcat.2024.115914.

Luo, Z., Wang, Y., He, M., Zhao, C., 2016. Precise oxygen scission of lignin derived aryl ethers to quantitatively produce aromatic hydrocarbons in water. Green Chem. 18, 433–441. https://doi.org/10.1039/C5GC01790D.

Lv, W., Hu, X., Zhu, Y., Xu, Y., Liu, S., Chen, P., Wang, C., Ma, L., 2022. Molybdenum oxide decorated Ru catalyst for enhancement of lignin oil hydrodeoxygenation to hydrocarbons. luoPreciseOxygenScission2016 188, 195–210. doi:10.1016/j.renene.2021.12.148.

Perdew, J.P., Burke, K., Ernzerhof, M., 1996. Generalized gradient approximation made simple. Phys. Rev. Lett. 77, 3865–3868. https://doi.org/10.1103/PhysRevLett.77.3865.

Pérez, E., Tuck, C.O., Poliakoff, M., 2018. Valorisation of lignin by depolymerisation and fractionation using supercritical fluids and conventional solvents. J. Supercrit. Fluids 133, 690–695. https://doi.org/10.1016/j.supflu.2017.07.033.

Polierer, S., Jelic, J., Pitter, S., Studt, F., 2019. On the reactivity of the Cu/ZrO_2 system for the hydrogenation of CO_2 to methanol: a density functional theory study. J. Phys. Chem. C 123, 26904–26911. https://doi.org/10.1021/acs.jpcc.9b06500.

Rigo, D., Fechter, T., Capanema, E., Diment, D., Alopaeus, M., Tarasov, D., Cantero, D., Balakshin, M., 2025. Isolation of β-O-4-rich lignin from birch in high yields enabled by continuous-flow supercritical water treatment. ChemSusChem 18, e202401683. https://doi.org/10.1002/cssc.202401683.

Rohrbach, A., Hafner, J., 2005. Molecular adsorption of NO on NiO(100): DFT and DFT + U calculations. Phys. Rev. B 71, 045405. https://doi.org/10.1103/PhysRevB.71.045405.

Salam, M.A., Cheah, Y.W., Ho, P.H., Olsson, L., Creaser, D., 2021. Hydrotreatment of lignin dimers over NiMoS-USY: effect of silica/alumina ratio. Sustainable Energy Fuels 5, 3445–3457. https://doi.org/10.1039/D1SE00412C.

Shen, X.-J., Huang, P.-L., Wen, J.-L., Sun, R.-C., 2017. A facile method for char elimination during base-catalyzed depolymerization and hydrogenolysis of lignin. Fuel Process. Technol. 167, 491–501. https://doi.org/10.1016/j.fuproc.2017.08.002.

Shen, Z., Shi, C., Liu, F., Wang, W., Ai, M., Huang, Z., Zhang, X., Pan, L., Zou, J., 2024. Advances in heterogeneous catalysts for lignin hydrogenolysis. Adv. Sci. 11, 2306693. https://doi.org/10.1002/advs.202306693.

Shu, R., Long, J., Xu, Y., Ma, L., Zhang, Q., Wang, T., Wang, C., Yuan, Z., Wu, Q., 2016. Investigation on the structural effect of lignin during the hydrogenolysis process. Bioresour. Technol. 200, 14–22. https://doi.org/10.1016/j.biortech.2015.09.112.

Sun, M.Z., Dougherty, A.W., Huang, B.L., Li, Y.L., Yan, C.H., 2020. Accelerating atomic catalyst discovery by theoretical calculations-machine learning strategy. Adv. Energy Mater. 10. https://doi.org/10.1002/aenm.201903949.

Toyoda, K., Nakano, Y., Hamada, I., Lee, K., Yanagisawa, S., Morikawa, Y., 2009. First-principles study of benzene on noble metal surfaces: adsorption states and vacuum level shifts. Surf. Sci. 603, 2912–2922. https://doi.org/10.1016/j.susc.2009.07.039.

Wang, C., Lv, J., Guo, X., Wei, W., Zhang, D., Zhang, Y., Li, H., Zhao, Y., 2025. Controllable synthesis of a porous flower-like Ni-NiO heterojunction catalyst for the hydrogenation of maleic anhydride: synergistic effects of metal and oxygen vacancies. ACS Catal. 15, 2961–2976. https://doi.org/10.1021/acscatal.4c06675.

Wang, V., Xu, N., Liu, J.-C., Tang, G., Geng, W.-T., 2021. VASPKIT: a user-friendly interface facilitating high-throughput computing and analysis using VASP code. Comput. Phys. Commun. 267, 108033. https://doi.org/10.1016/j.cpc.2021.108033.

Wang, X., Yang, C., Wang, P., Shen, C., 2023. Small interface with ample impact: synergistic catalysis between Ni0 and Ni2+ during nitrobenzene hydrogenation. Chem. Eng. J. 470, 144195. https://doi.org/10.1016/j.cej.2023.144195.

Wen, Y., Zormpa, F., Sharapa, D.I., Studt, F., Raffelt, K., Dahmen, N., 2025. Exploring the hydrodeoxygenation of lignin β-O-4 dimer model compound and bio-oil by DFT and experimental studies. Mol. Catal. 580, 115134. https://doi.org/10.1016/j.mcat.2025.115134.

Whittaker, T., Kumar, K.B.S., Peterson, C., Pollock, M.N., Grabow, L.C., Chandler, B.D., 2018. H_2 oxidation over supported Au nanoparticle catalysts: evidence for heterolytic H_2 activation at the metal–support interface. J. Am. Chem. Soc. 140, 16469–16487. https://doi.org/10.1021/jacs.8b04991.

Xin, X., Li, Z., Chi, M., Zhang, M., Dong, Y., Lv, H., Yang, G.-Y., 2023. A recoverable polyoxometalate-ionic liquid catalyst for selective cleavage of lignin β-O-4 models under mild conditions. Green Chem. 25, 2815–2824. https://doi.org/10.1039/D3GC00087G.

Xu, C., Tang, S.-F., Sun, X., Sun, Y., Li, G., Qi, J., Li, X., Li, X., 2017. Investigation on the cleavage of β-O-4 linkage in dimeric lignin model compound over nickel catalysts supported on ZnO-Al_2O_3 composite oxides with varying Zn/Al ratios. Catal. Today 298, 89–98. https://doi.org/10.1016/j.cattod.2017.05.048.

Xu, Y., Yao, J., Lin, H., Lv, Q., Liu, B., Wu, L., Tan, L., Dai, Y., Zong, X., Tang, Y., 2024. Functional CeO_x stabilized metallic Ni catalyst supported on boron nitride for durable partial oxidation of methane to syngas at high temperature. ACS Catal. 14, 11845–11856. https://doi.org/10.1021/acscatal.4c01055.

Xue, Z., Yu, H., He, J., Zhang, Y., Lan, X., Liu, R., Zhang, L., Mu, T., 2020. Highly efficient cleavage of ether bonds in lignin models by transfer hydrogenolysis over dual-functional ruthenium/montmorillonite. ChemSusChem 13, 4579–4586. https://doi.org/10.1002/cssc.202000978.

Yang, Z., Luo, B., Shu, R., Zhong, Z., Tian, Z., Wang, C., Chen, Y., 2022. Synergistic effect of active metal–acid sites on hydrodeoxygenation of lignin-derived phenolic compounds under mild conditions using Ru/C-HPW catalyst. Fuel 319, 123617. https://doi.org/10.1016/j.fuel.2022.123617.

Zhang, X., Yan, H., Zhu, L.J., Li, T., Wang, S.R., 2020. Hydrodeoxygenation of lignin-derived monomers and dimers over a Ru supported solid super acid catalyst for cycloalkane production. Adv. Sustainable Syst. 4. https://doi.org/10.1002/adsu.201900136.

Zhao, B., Wang, Z., Liu, Z., Yang, X., 2016. Two-stage upgrading of hydrothermal algae biocrude to kerosene-range biofuel. Green Chem. 18, 5254–5265. https://doi.org/10.1039/c6gc01413e.

Zhao, Z.-J., Li, Z., Cui, Y., Zhu, H., Schneider, W.F., Delgass, W.N., Ribeiro, F., Greeley, J., 2017. Importance of metal-oxide interfaces in heterogeneous catalysis: a combined DFT, microkinetic, and experimental study of water-gas shift on Au/MgO. J. Catal. 345, 157–169. https://doi.org/10.1016/j.jcat.2016.11.008.

Zhou, H., Liu, J., Chen, D., Qin, Y., Wang, T., Qiu, X., Lin, X., 2025. Boosting middle hydroxyl adsorption on lignin-derived carbon loaded MnO–Ni for glycerol conversion to dihydroxyacetone. AIChE J 71, e70012. https://doi.org/10.1002/aic.70012.

Zhou, M., Chen, C., Liu, P., Xia, H., Li, J., Sharma, B.K., Jiang, J., 2020. Catalytic hydrotreatment of β-O-4 ether in lignin: cleavage of the C–O Bond and hydrodeoxygenation of lignin-derived phenols in one pot. ACS Sustain. Chem. Eng. 8, 14511–14523. https://doi.org/10.1021/acssuschemeng.0c04941.